# Anisotropic Gold Nanomaterial Synthesis Using Peptide Facet Specificity and Timed Intervention

Kacper J. Lachowski, $^{\dagger,\ddagger}$  Huat Thart Chiang, $^{\dagger}$  Kaylyn Torkelson, $^{\dagger}$  Wenhao Zhou, $^{\P,\S}$  Shuai Zhang, $^{\P,\S,\ddagger}$  Jim Pfaendtner, $^{\dagger}$  and Lilo D. Pozzo\*, $^{\dagger,\ddagger,\P}$ 

†Department of Chemical Engineering, University of Washington, Seattle, WA 98105. ‡Molecular Engineering and Sciences Institute, University of Washington, Seattle, WA 98105.

¶Department of Material Science and Engineering, University of Washington, Seattle, WA
98105.

§Physical Sciences Division, Pacific Northwest National Laboratory, Richland, WA 99352.

E-mail: dpozzo@uw.edu

#### **Abstract**

Thin metal particles with two-dimensional symmetry are attractive for multiple applications, but are difficult to synthesize in a reproducible manner. Although molecules that selectively adsorb to facets have been used to control nanoparticle shape, there is still limited research into the temporal control of growth processes to control these structural outcomes. Moreover, much of the current research into the growth of thin two-dimensional particles lacks mechanistic details. In this work, we study why the substitution of isoleucine for methionine in a gold binding peptide (Z2, RMRMKMK) results in an increase in gold nanoparticle anisotropy. Nanoplatelet growth in the presence of Z2M246I (RIRIKIK) is characterized using *in situ* small-angle X-ray scattering (SAXS) and UV-Vis spectroscopy. Fitting time-resolved SAXS profiles reveals that 10

nm thick particles with two-dimensional symmetry are formed within the first few minutes of the reaction. Next, through a combination of electron diffraction and molecular dynamics simulations, we show that substitution of methionine for isoluecine increases the (111) facet selectivity in Z2M246I, and conclude that this is key to the growth of nanoplatelets. However, the potential application of nanoplatelets formed using Z2M246I is limited due to their uncontrolled lateral growth, aggregation, and rapid sedimentation. Therefore, we use a liquid handling robot to perform temporally controlled synthesis and dynamic intervention through the addition of Z2 to nanoplatelets growing in the presence of Z2M246I at different times. UV-Vis spectroscopy dynamic light scattering, and electron microscopy show that dynamic intervention results in control over the mean-size and stability of plate-like particles. Finally, we use in situ UV-Vis spectroscopy to study plate-like particle growth at different times of intervention. Our results demonstrate that both the selectivity and magnitude of binding free energy towards lattices is important for controlling nanoparticle growth pathways.

## Introduction

Anisotropically shaped plasmonic nanoparticles such as nanoplates, nanorods, and various morphologies with protruding morphologies exhibit a longitudinal plasmon resonance mode that is not present in spherical nanoparticles. <sup>1–6</sup> A unique feature of particles with two dimensional symmetry is that the ratio of extinction from transverse and longitudinal modes decreases with decreasing thickness. <sup>3</sup> The position of the longitudinal surface plasmon resonance (SPR) peak can be tuned to near-infrared wavelengths by changing the associated characteristic dimension (e.g. nanorod length, nanotriangle edge length). This is desirable for biomedical applications that take advantage of the low optical extinction of tissues in the near-infrared range. <sup>7</sup> However, particles with two dimensional symmetry need to be thin to exhibit optical extinction in the near-infrared spectrum, be synthetically accessible, and colloidally stable. <sup>3</sup> An added benefit of thin plasmonic structures is that they have a high

specific surface area, which is advantageous for catalysis applications.<sup>8</sup> Surface enhanced Raman spectroscopy (SERS) is another application in which anisotropic particles outperform spherical particles.<sup>2,4,9,10</sup> Besides particle anisotropy, the presence of nanoscale tips or gaps leads to an enhancement of the electromagnetic field due to local hotspots and is beneficial to SERS and photocatalysis applications of colloidal nanoparticles.<sup>10,11</sup> Methods for synthesizing colloidally stable metal nanoparticles that are thin, have two dimensional symmetry, and irregularly shaped edges often require etching of existing plate-like particles which adds additional synthesis steps.<sup>2,4</sup> This is not optimal given that many syntheses of two-dimensional metal nanomaterials are based on growth of seed particles, which is already a two-step process. Alternative methods that do not require multiple processing steps have been identified in the literature and we point the readers to a recently published review on the subject.<sup>12</sup> On the other hand, as the authors point out, there are limited examples of in situ characterization methods being applied to the formation process of two-dimensional metal nanomaterials.<sup>12</sup>

An under-appreciated experimental parameter in two-dimensional nanomaterial synthesis, which has been applied to anisotropic nanoparticle synthesis in the past, is the time at which a certain reagent is added to the synthesis. The use of this approach has been limited by its complexity as well as the practical challenges of manually intervening in a time controlled manner by experimenters. Quenching reactions at different times with the addition of metal ion scavenging molecules is a basic example of temporal control that can improve stability and alters nanoparticle structure.<sup>5,6</sup> In another work, a small molecule that bound selectively to gold facets was used to partially reduce HAuCl<sub>4</sub> before addition of the strong reducing agent sodium borohydride.<sup>1</sup> By changing the length of the incubation step, the authors were able to control the characteristic dimensions of highly anisotropic gold nanoparticles such as nanopods. A more sophisticated approach to growing Au–Ag nanostructures was also recently reported by Wang et al.<sup>13</sup> The authors observed that different particle morphologies were formed in the presence of two different DNA sequences. Particles

were grown in the presence of one sequence for different amounts of time, ligand exchange was performed to replace the first sequence for the other, and particle growth was resumed by addition of new precursor. Again, the time at which the synthetic intervention took place allowed for predictive control over particle structure. While temporal control is fundamental to biomineralization, bioinspired nanomaterial syntheses using sequence defined molecules often dispense with this potential for synthetic control by adding all reagents simultaneously.

In our previous work, we identified that substitution of methionine with the physicochemically similar, but chemically dissimilar isoleucine, led to dramatically different nanoparticle synthesis outcomes. Specifically, we identified that anisotropic, interconnected, and platelike gold nanomaterials were formed in the presence of Z2M246I. 14 However, the plate-like particles were not colloidally stable, and varying the reagent concentration was not effective at limiting the lateral dimension of the plate-like particles. In this work we set out to understand the formation mechanism, and to control the colloidal stability and lateral dimension of the nanoplatelets. In addition to electron microscopy and AFM imaging studies, in situ UV-Vis and small-angle X-ray scattering were used to study the formation of anisotropic structures in the presence of Z2M246I. We couple our experimental findings with meta molecular dynamics simulations to assess the effect of methionine substitution on peptide facet selectivity of the peptide Z2M246I (RIRIKIK). Next, we programmed a liquid-handling robot to dynamically intervene in the synthesis by adding Z2 (RMRMKMK) at different times. The latter peptide was previously observed to form highly stable spherical nanoparticles in a wide range of conditions. 14 We hypothesized that addition of Z2 at different times would cap the lateral growth of anisotropic particles being formed in the presence of Z2M246I, and thereby achieve control over the lateral dimension and colloidal stability of plate-like nanoparticles. A microplate based sedimentation assay inspired by another publication <sup>15</sup> was used to screen for synthesis conditions that met our design objectives: formation of plate-like particles and an improvement in colloidal stability relative to the control in which no intervention had taken place. We used UV-Vis spectra of the plasmonic nanoparticles as a proxy for changes in structure and sedimentation. Once the desired synthesis conditions were identified, and the stability of the samples was corroborated using a cuvette based sedimentation assay, we used electron microscopy, AFM, and dynamic light scattering to identify how the time of addition of Z2 changes the resulting structures. Finally, we obtain *in situ* UV-Vis spectroscopy to identify changes in the assembly mechanism when intervention takes place at different times, and comment on the importance of methionine in this system.

## **Experimental Materials and Methods**

#### **Materials**

All peptides were synthesized by Biomatik Corporation (Cambridge, ON, Canada), purified using HPLC to > 95% purity by the manufacturer, and the lyophilized trifluoroacetate salt was used without further modification. The previously described peptide Z2 (RM-RMKMK), <sup>16</sup> was modified by substituting methionine at different positions in the sequence for isoleucine. Z2M6I refers to the amino acid sequence RMRMKIK in which methionine residue in the sixth position in the sequence is substituted for isoleucine. All of the peptide sequences are also presented in Table 1.

Table 1: Peptide Nomenclature

Peptide Name	Sequence
Z2	RMRMKMK
Z2M6I	RMRMKIK
Z2M46I	RMRIKIK
Z2M246I	RIRIKIK

Gold chloride trihydrate ( $\text{HAuCl}_4 \cdot 3\,\text{H}_2\text{O} \geq 99.9\%$ ) was obtained from Sigma-Aldrich (St. Louis, MO, USA). 4-(2-hydroxyethyl)-1-piperazineethanesulfonic acid (HEPES) was obtained from EMD Chemicals (Gibbstown, NJ, USA). Ultra-pure water used in the study was obtained from a Direct-Q 3 UV water purification system with a resistivity of 18.2  $M\Omega$  (Millipore Corporation, Bedford, MA, USA).

#### Sample Preparation and Dynamic Intervention

Aqueous stock solutions of HAuCl<sub>4</sub> (10 mM), HEPES (3 mM), and peptide (0.3 mM) were prepared before each synthesis. Samples used in UV-Vis, imaging, and DLS studies were all prepared using an OT-2 liquid handling robot (Opentrons, Brooklyn, NY, USA), and samples were prepared manually for *in situ* SAXS and UV-Vis studies. Except where indicated otherwise, final sample concentrations were 0.4 mM HAuCl<sub>4</sub>, 1.0 mM HEPES, 0.08 mM of Z2M246I (RIRIKIK), and 0.08 mM of Z2 (RMRMKMK). The order in which stocks were added was water, HEPES, Z2M246I, HAuCl<sub>4</sub>, and Z2. A custom Python script (OTTO, https://github.com/pozzo-research-group/otto) was used to control the time at which the Z2 peptide was added relative to HAuCl<sub>4</sub>. Samples were prepared in 48-well Falcon microplates (Corning, Corning, NY, USA). For the microplate based sedimentation assay, 200 μL of the sample was automatically transferred to a 96-well plate (Corning, Corning, NY, USA) immediately after all pipetting steps were completed, and then again after a delay period of 12-15 hours to allow for sedimentation to take place. For the cuvette based sedimentation assay, samples were transferred to polystyrene cuvettes after all pipetting steps were completed.

#### Zeta Potential

Zeta potential measurements were performed on a Malvern Panalytical (Malvern, United Kingdom) Zetasizer Nano ZS. Three zeta potential measurements were performed and averaged to obtain the reported zeta potential value. Measurements were performed in a folded capillary zeta cell.

#### **UV-Vis Characterization**

UV-Vis measurements of samples in microplates were obtained using an Epoch 2 microplate spectrophotometer (BioTek, Winooski, VT, USA), and a Thermo Scientific Evolution 300 (Waltham, MA, USA) was used to characterize samples in cuvettes. *in situ* UV-Vis measurements were carried out in a 48-well microplate format. In all cases data normalization was performed by subtracting absorbance of water measured in the same format.

#### In Situ SAXS Experiments and Data Fitting

SAXS measurements were obtained using a Xeuss 3.0 (Xenocs, Grenoble, France) under vacuum and characterized using Cu  $K_{\alpha}$  radiation. The reagent concentrations used were 0.04 mM Z2M246I, 0.2 mM HAuCl<sub>4</sub>, and 1 mM HEPES. All reagents were mixed in a centrifuge tube except for HAuCl<sub>4</sub>. Next, a cycle of image collection at a 90 cm sample to detector distance with 2 minute exposures was initiated, the precursor was rapidly added to the tube and agitated, and the start time was recorded. The sample was then injected using a syringe into a custom built sample holder located inside the instrument as described in the Supporting Information. Data reduction was performed in XSACT software (Xenocs, Grenoble, France) by azimuthally integrating 2D images to obtain 1D scattering profiles. A water background measurement collected in the same sample holder was subtracted.

Reduced data at each time point were fit using a Guinier-Porod model<sup>17</sup> (see Supporting Information for additional details). This model enables fitting of arbitrary particle shapes by applying a continuity between the Guinier and Porod regions of scattering that correspond to scattering at low-q and high-q, respectively. The combined Guinier-Porod model includes a dimension parameter to account for power-law scattering of non-spherical particles in the intermediate Guinier region. Scattering in the intermediate Guinier region of particles with two-dimensional symmetry will lead to a dimension parameter of 2, and the corresponding radius of gyration is related to the thickness of the particles by  $T = R_g \sqrt{12}$ . Model fitting was performed using the Sasview/sasmodels package for Python.<sup>18</sup>

## Electron Microscopy

Scanning electron microscopy (SEM) was performed using an Apreo-S (Thermo Fisher, Waltham, MA, USA). Samples in microplates were re-suspended by pipetting up and down,  $5 \mu L$  aliquots were deposited on clean silicon wafers, and dried overnight. The instrument was operated at 1 kV and 3.1 pA, and images were obtained from in-lens detectors.

For transmission electron microscopy (TEM), samples were also re-suspended, 5  $\mu L$  was cast on square carbon coated, 200 mesh, copper grids obtained from Electron Microscopy Sciences (Hatfield, PA, USA), and dried overnight. Imaging and Selected area electron diffraction (SAED) were performed using a Tecnai G2 F20 SuperTwin TEM instrument operated at 200 kV.

## **Atomic Force Microscopy**

Atomic force microscopy (AFM) imaging was carried out on samples prepared in the same way as for SEM. Samples were characterized using a Dimension Icon AFM (Bruker, CA, USA) in air using PeakForce QNM mode and ScanAsyst-Air probes (Bruker, CA, USA). Image processing and particle dimension analysis was performed using Gwyddion. <sup>19</sup> Line-profile measurements for samples in which Z2 was added are shown in the Supporting Information (Figures S1-S7).

## Dynamic Light Scattering

Dynamic light scattering (DLS) measurements were taken on a Malvern Panalytical (Malvern, United Kingdom) Zetasizer Nano ZS. Samples used were prepared using the liquid-handling robot as previously described, and were transferred to polystyrene cuvettes without dilution. The intensity weighted peak distribution of diffusion coefficients is presented rather than the hydrodynamic diameter, because the latter requires the assumption that the particle shape is spherical. The highest intensity peak obtained from each synthesis condition is

also converted to an equivalent diameter depending on whether it can be attributed to either spherical nanoparticles or nanoplatelets. Hernández-Cifre et al.  $^{20}$  developed an expression for estimating the diffusion coefficient for various nanoplatelet particles. The equivalent diameter of a peak assigned to nanoplatelets is obtained by first solving for the area A in the expression for the friction coefficient f obtained from the cited work:  $^{20}$ 

$$f = 12\eta_0 \left( \sqrt{\frac{A}{\pi}} C + Qh \right) \tag{1}$$

Where  $\eta_0$  is the viscosity of the medium, h is nanoplatelet thickness (estimated to be 10 nm based on experimental results), and C and Q are fitting parameters for hexagonal nanoplatelets obtained from numerical simulations.<sup>20</sup> The width of a hexagon with the obtained area is then used to estimate changes in nanoplatelet diameter.

#### **Molecular Simulations**

The initial configurations for the peptides were constructed in GaussView<sup>21</sup> using the amino acid fragment library with an  $NH_2$  N-terminus and a COOH C-terminus. The PDB and ITP files for the Au(100) and the Au(111) slab were taken from prior work by Qi et al.<sup>22</sup> The CHARMM36 force field (FF)<sup>23,24</sup> was used to describe each peptide while the GolP-CHARMM FF<sup>25</sup> was used to describe the Au-Au and Au-Solution interactions in conjunction with the TIP3P water model.<sup>26</sup> This forcefield has been experimentally validated to reproduce the facet selectivity of peptides binding to gold.

We solvated each peptide-surface system using Packmol<sup>27</sup> with explicit water, 10 Na+ions, and 14 Cl<sup>-</sup> ions to neutralize the charge. All molecular dynamics simulations were conducted using GROMACS<sup>28</sup> with the PLUMED plugin<sup>29</sup> for enhanced sampling. The LINCS algorithm was used to constrain bonds between hydrogens and heavy atoms so that a 2 femtosecond timestep could be used. Lennard Jones and Coulombic interactions were calculated with a cutoff of 1.0 nm and long-range electrostatic interactions were treated with

the Particle Mesh Ewald method. All systems underwent energy minimization using the steepest descent algorithm for a maximum of 10 picoseconds followed by NPT equilibration using a stochastic velocity rescaling thermostat<sup>30</sup> (298 K) and the Berendsen barostat<sup>31</sup> (1 bar) for 5 ns, with pressure coupling only applied to the z-dimension. The final frame of this NPT equilibration was used to start a 100-nanosecond unbiased NVT simulation at 298K and from this trajectory we selected four different configurations to serve as starting configurations for different replicas in the production simulations. We froze the position of all Au atoms during EM, NPT, and NVT steps according to previous recommendations.<sup>25</sup>

Parallel-bias metadynamics (PBMetaD)<sup>32</sup> with multiple walkers<sup>33</sup> and adaptive gaussians<sup>34</sup> was used to calculate the binding free energy for each peptide on each surface. PBMetaD allows biasing of multiple collective variables (CVs) in parallel to encourage efficient exploration of the free energy landscape. We biased nine one-dimensional CVs in each PBMetaD calculation, including the center of mass (COM) z-distance between the peptide backbone and the surface, the COM z-distance between each sidechain head group and the surface, and the radius of gyration. Each production simulation consists of four walkers with 1 microsecond of sampling per walker, for a total of 4 microseconds of simulation time needed to reach convergence. Standard tests of convergence were performed and presented in the SI. The PLUMED input files required to reproduce these results are available on PLUMED-NEST (www.plumed-nest.org), the public repository of the PLUMED consortium, as plumID:23.018.<sup>35</sup>

## Results and discussion

## Morphogenesis of Interconnected Nanoplatelets

Studies of methionine containing peptides identify that the residue contributes significantly to the binding of peptides to gold surfaces.<sup>36,37</sup> All three methionines in the rationally designed Z2 sequence (RMRMKMK)<sup>16</sup> were predicted to make significant contact with gold

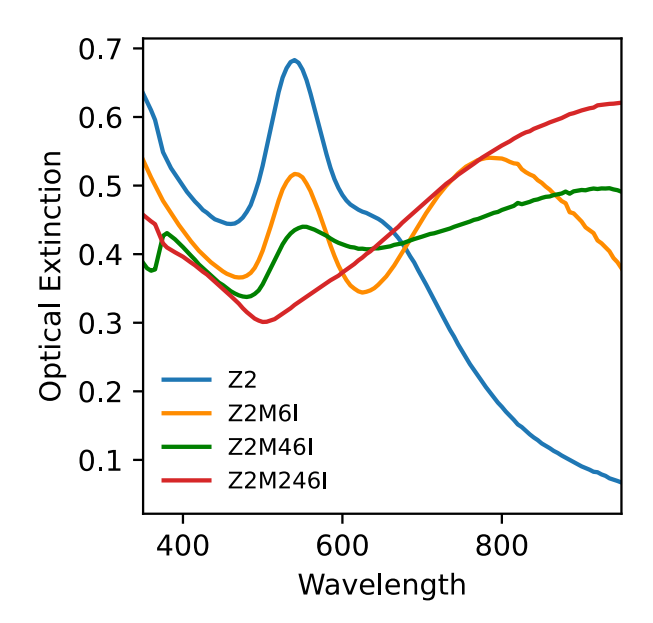


Figure 1: UV-Vis spectra of Au nanoparticles formed using 0.2 mM HAuCl<sub>4</sub>, 0.1 mM HEPES, and 0.04 mM of peptide. Peptides used were variants of the peptide sequence Z2 (RMRMKMK) with different methionines substituted for isoleucine: Z2M6I (RMRMKIK), Z2M46I (RMRIKIK), and Z2M246I (RIRIKIK). Increasing the amount of methionines substituted for isoleucine in the Z2 sequence leads to a red shift in the plasmon resonance peak position at higher wavelengths indicating that larger plates are being formed.

surfaces by molecular dynamics studies.<sup>36</sup> Additionally, methionine plays a role in chemical reduction of gold because it can be oxidized and form intermediate Au(I)-methionine species.<sup>38</sup> It has been proposed that Au(I)-methionine complexation may decrease the rate of reduction,<sup>37</sup> and impede secondary nucleation on or near the particle surface.<sup>39</sup> The former is evident in our previous work which explored the effect of substituting methionine with isoleucine in the Z2 sequence.<sup>14</sup> We observed that increasing the concentration of methionine containing Z2 variants decreased the concentration of Au(0) 1 day after synthesis based on absorbance at 400 nm, which is proportional to the concentration of Au(0).<sup>40</sup> In contrast, increasing the concentration of the Z2M246I sequence, with all three methionines substituted for isoleucine, did not decrease the apparent concentration of Au(0) after 24 hours. Moreover, we observed that decreasing the number of methionines led to an incremental increase in particle anisotropy. This can be seen in Figure 1, which shows spectra of gold nanomaterials formed in the presence of variants with increasing numbers of methionine

substitutions. We note that adsorption of any of the peptide variants to gold surfaces should provide a similar degree of colloidal stabilization via electrostatic repulsion due to positively charged lysine and arginine side chains. This is supported by the expected isoelectric point of approximately 12 for all of the sequences, and a zeta potential value of 16.8 mV at a pH of 3.3 for spherical particles stabilized by Z2. Nevertheless, differences in peptide chemistry and interaction with particles results in differences in particle growth outcomes. While Z2 shows one LSPR peak corresponding to spherical nanoparticles, the remaining variants show contributions from LSPR at higher wavelengths, which is consistent with the longitudinal plasmon resonance mode of plate-like particles identified in the samples using electron microscopy as demonstrated in our previous work and in Figure 2 A. No LSPR peak related to spherical particles could be observed in a wide range of synthesis conditions in the presence of Z2M246I. <sup>14</sup> The SEM image in Figure 2 A of a sample formed in the presence of Z2M246Ishows aggregates of anisotropic plate-like particles with irregular edges. A TEM image of a similar group of particles with irregular edges and somewhat triangular shape is shown in Figure 2 B. The apparent wrinkle-like defects and translucence of the plate-like particles suggests that they are relatively thin with respect to their width. Plate-like particles may exhibit transverse and lateral modes of plasmon resonance which are affected by the thickness and lateral dimension of the particle. However, the surface plasmon resonance of thin disc-like gold particles is predicted<sup>3</sup> to have minor contributions from the transverse mode, leading to only one LSPR peak as observed for Z2M246I in Figure 1. The particles formed in the presence of Z2M246I were identified to be 10 nm thick using AFM as shown in Figure 3. Selected area electron diffraction and FFT analysis of HR-TEM images shown in Figure 2 are consistent with (111) basal facets based on the presence of  $\{220\}$  and  $\frac{1}{3}\{422\}$ reflections. 41,42 The latter have been attributed to different types of stacking faults in metal nanoplates 42 and have a 2.5 Å interplanar spacing that was also identified in the FFT of plate-like particle surfaces in the sample. Each of these stacking faults may contribute to anisotropic growth in the [100] direction, and may form as a result of a molecule selectively

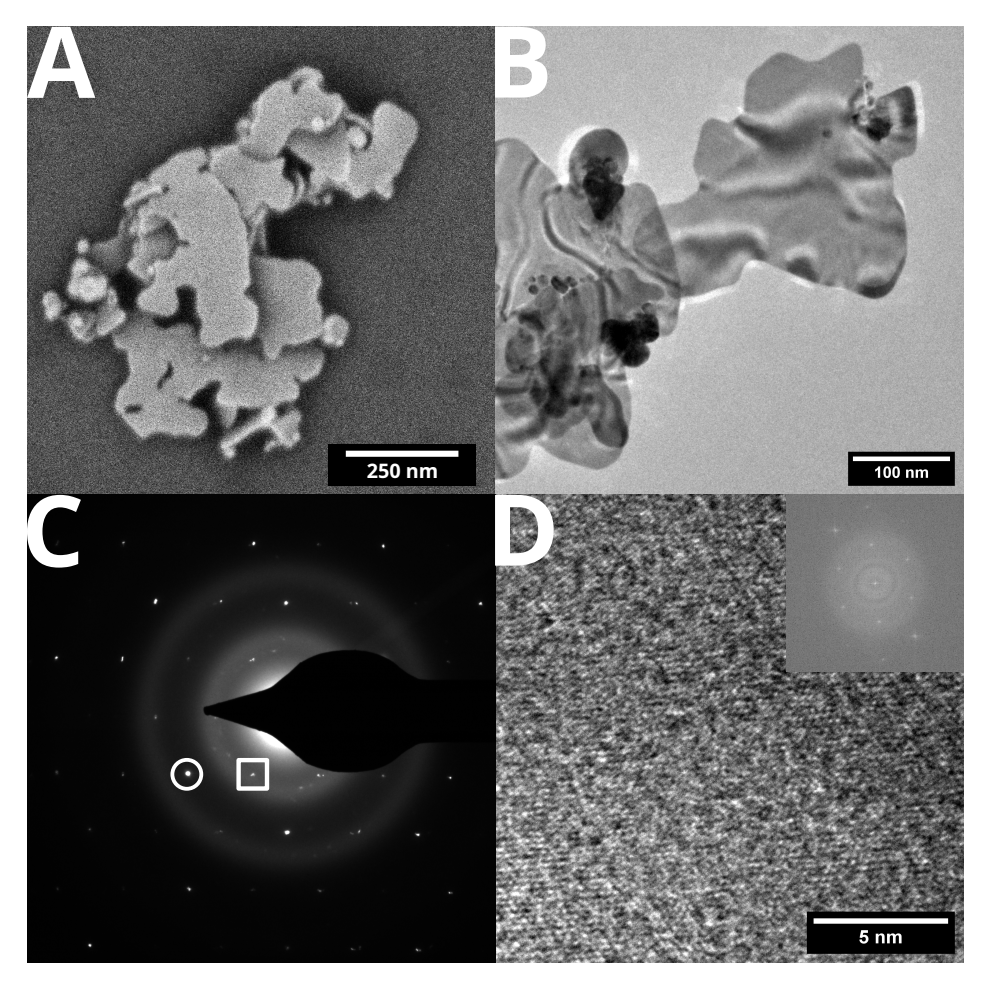


Figure 2: A SEM of an aggregate of irregularly shaped plate-like and spherical particles. B TEM of samples prepared in presence of Z2M246I. Presence of wrinkle-like defects suggests that the structures are thin. C SAED of the basal facet of an isolated plate-like particle which was indexed as the [111] direction. Points in the circle and square are from  $\{220\}$  and  $1/3\{422\}$  reflections, respectively. D and the inset figure correspond to an HRTEM image and its FFT of a plate-like structure, respectively. The inner ring of points corresponds to 0.25 nm interplanar spacing which is consistent with reflections from  $\frac{1}{3}\{422\}$ .

binding to the (111) facet. 42

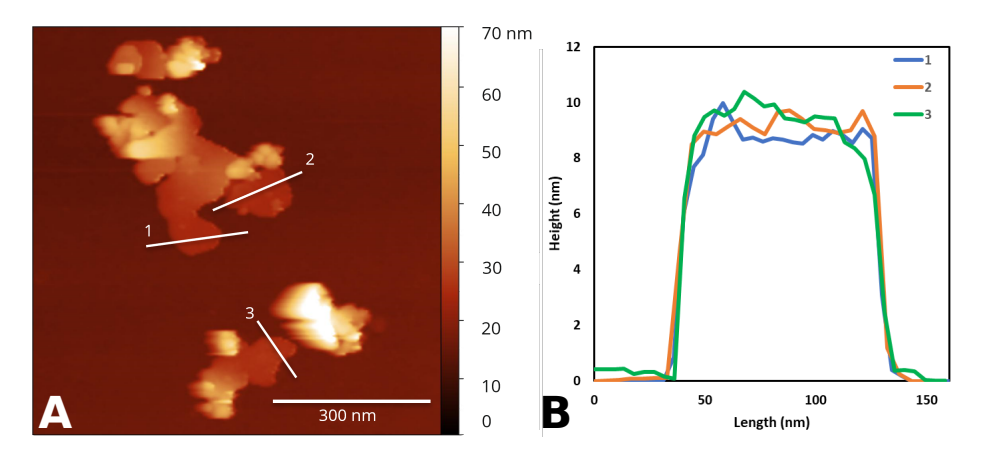


Figure 3: A AFM image showing plate-like particles with an approximate thickness of 10 nm, as indicated by the annotations and the corresponding line-profiles in B.

Time-resolved SAXS curves of nanoparticle growth in the presence of Z2M246I are shown in Figure 4. The low-q limit of the instrumental configuration is limited to ca.  $0.007 \text{ Å}^{-1}$ which restricts the measurement to structures with dimensions smaller than ca. 90 nm. The scattering profile at each time point was fit using a Guinier-Porod model<sup>17</sup> and is described in the methods section. As seen in Figure 4 B, the fitted dimension parameter reaches a value of 2 after ca. 10 minutes, indicating that a symmetry breaking event occurs before this time, and results in plate-like particle growth. The corresponding radius of gyration in each fit is converted to thickness and plotted in Figure 4 C, and is approximately 10 nm. The thickness is consistent with the AFM results of particles that were cast several hours after the start of synthesis as shown in Figure 3. Given that the (111) facet is exposed on the plate-like particles observed using TEM, we concluded that there must be a mechanism that limits the thickness of particles by preventing growth in the [111] direction. Furthermore, we believe that this is related to the difference between how Z2 and Z2M246I interact with gold precursors and the surface of particles. Amino acids containing aromatic or sp<sup>2</sup> hybridized atoms, such as arginine, were identified to have a higher preference for binding to (111) vs (100) facets in MD simulations. 43 Similarly, proteins selected on the basis of preferential binding to gold (111) facets using directed evolution displayed a high frequency of lysine and arginine.<sup>44</sup> While methionine is also known to have a strong binding energy to gold surfaces, we have not found literature supporting the selectivity of methionine for (111) surfaces. Therefore, we hypothesized that in the absence of methionine, the remaining arginine and lysine residues in Z2M246I result in a higher preference for binding to the (111) facet of gold nanomaterials during synthesis. As a result, the (111) facet is stabilized, stacking faults are created, and growth occurs preferentially in the [100] direction. The facet selectivity of Z2 and Z2M246I are examined using molecular dynamics simulations in the next section.

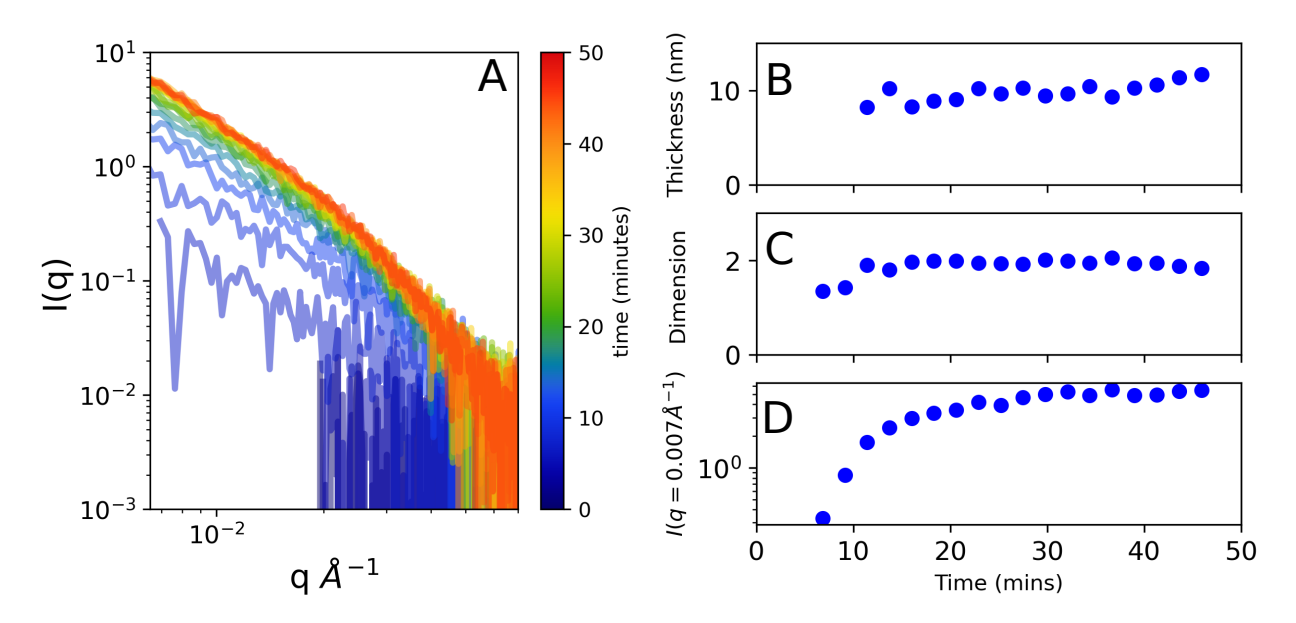


Figure 4: A Time-resolved SAXS profiles characterizing the formation of Au structures formed using 0.04 mM Z2M246I, 0.2 mM HAuCl<sub>4</sub>, and 1 mM HEPES. Once the scattering intensity was sufficiently high to fit (approximately 10 minutes), the scattering profile at each point was fitted using a Guinier-Porod model, and the fit parameters were plotted as a function of time in B and C. The dimension variable increased to and stayed near a value of 2, and is consistent with plate-like structures. The radius of gyration of time points which had a dimension variable near 2 were converted to thickness, and demonstrated that the thickness plateaus to a value of approximately 10 nm. The intensity of scattering at low-q (q=0.007 Å<sup>-1</sup>) is proportional to the concentration of particles, and is stable after approximately 30 minutes.

#### **Molecular Dynamics Simulations**

Molecular dynamics simulations were used to calculate the free energy profile of Z2 and Z2M246I adsorbed on the Au(100) and the Au(111) surface as shown in Figure 5. Both peptides favor the Au(111) surface over the Au(100) surface, but the Z2 peptide binding is significantly stronger to both gold surfaces in comparison to the Z2M246I peptide. This is likely a result of the closer binding of methionine residues to each surface as compared to the isoleucine residues in Z2M246I.

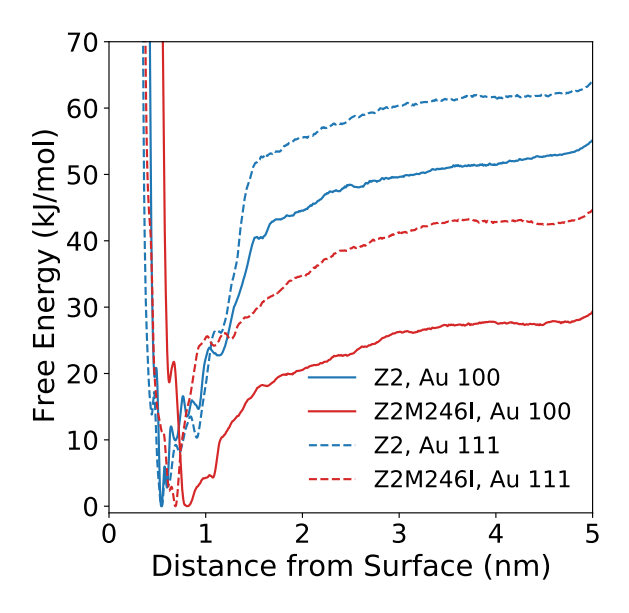


Figure 5: Free energy profiles for peptide adsorption on Au facets. The x-axis indicates the orthogonal distance of the center of mass (COM) of each peptide backbone from the surface while the y-axis indicates the free energy associated with that distance from the surface.

These free energy profiles can be converted to binding free energies according to standard practice.  $^{45,46}$  As shown in Table 2, this calculation yields a binding energy of  $52.5 \pm 0.15$  kJ/mol for Z2 to Au(111) and  $41.9 \pm 0.17$  for Z2 to Au(100), with errors being calculated as the standard deviation of the binding energy over the last 20% of the simulation time. The binding energy of Z2M246I to Au(111) is  $33.2 \pm 0.22$  kJ/mol and  $21.6 \pm 0.12$  kJ/mol for Z2M246I on Au(100). Additional details on calculating the binding free energies, validating the convergence of the calculation, and additional analyses are provided in the Supporting

Information (Figures S8-S13). The ratio of the binding energy to the Au(111) surface and the Au(100) surface can then be calculated as shown in Table 2. Z2M246I has a stronger preference for the Au(111) surface than the Z2 peptide does, providing support for the hypothesis that the modifications in Z2M246I lead to a higher preference for binding to the 111 facet of gold nanomaterials during synthesis.

Table 2: Tabulated binding energies for each peptide on each facet calculated using block averaging. Binding energies have been averaged over the last 20% of simulation time with error defined as the standard deviation over the same time frame.

Peptide	Au (111) (kJ/mol)	Au (100) (kJ/mol)	Au (111)/(100)
Z2	$52.5 \pm 0.15$	$41.9 \pm 0.17$	1.25
Z2M246I	$33.2 \pm 0.22$	$21.6 \pm 0.12$	1.54

## Dynamic Intervention Using Z2

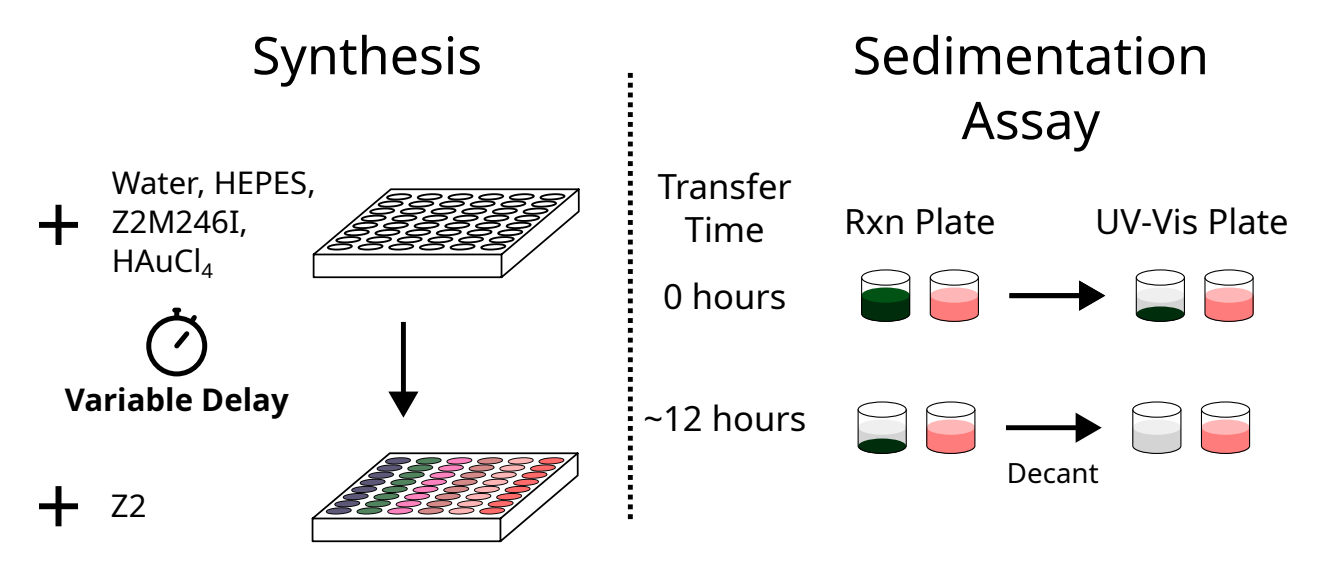


Figure 6: Overview of the synthesis and microplate sedimentation assays used in this section. Samples were synthesized using a liquid handling robot and custom script as described in the methods section. The sedimentation assay consists of two transfer steps in which 200  $\mu L$  aliquots are transferred from 600  $\mu L$  of sample in the 48-well reaction plate to wells in the 96-well plate used for UV-Vis characterization. Comparison of spectra from samples which were transferred immediately, or 12-15 hours after all synthesis steps were completed, allows for differentiation between extents of sedimentation between samples. For example, a sample that sediments significantly in the reaction plate during the 12-15 hour period will have much lower optical extinction in the second aliquot transferred to the microplate used in UV-Vis characterization relative to the first aliquot.

Given the preference that Z2M246I has for binding (111) facets, and the increase in anisotropic particles terminated by (111) facets, it is likely that Z2M246I is responsible for limiting growth in the [111] direction. However, the resulting nanoparticles are colloidally unstable and aggregate irreversibly after several days. We hypothesized that addition of Z2 during synthesis in the presence of Z2M246I would lead to more colloidally stable plate-like particles, because it has less selective binding and also has a stronger binding energy to either facet when compared to Z2M246I. In the proposed mechanism, Z2 added after the reaction has started should bind to facets with low Z2M246I coverage, such as (100), and limit lateral growth of plate-like structures. A liquid handling robot was used to prepare samples and add Z2 after a specified amount of time as described in the methods section and illustrated in Figure 6. We expected to cap the growth of nascent plate-like particles by adding Z2 at different times. Samples were created in one microplate (reaction plate) and then transferred to another microplate (characterization plate). Transfer of samples from the reaction plate to the characterization plate was repeated the following day (12-15 hours). This proved to be a fast method of determining which sample conditions resulted in colloidally unstable gold nanoparticles by comparing the decanted sample taken right after the reaction was started, and after samples were allowed to sediment (see Figure 6 for details).

The UV-Vis spectra in Figure 7 A and B show the samples transferred before and after sedimentation had time to occur, respectively. The spectra of the control sample prepared in the absence of Z2 show minimal optical extinction after decanting and demonstrate that the particles sedimented in the reaction plate. Samples in which Z2 was added early on in the reaction, such as after 1, 3, or 5 minutes, feature only one LSPR peak, and are therefore consistent with spherical particles. The spectra of these three samples were similar independent of the time that they were transferred, and demonstrate that the particles formed were colloidally stable. Addition of Z2 after more than 5 minutes resulted in an increase in optical extinction at higher wavelengths, and a decrease in the optical extinction of the first LSPR peak. Optical extinction at higher wavelengths indicates that plate-like

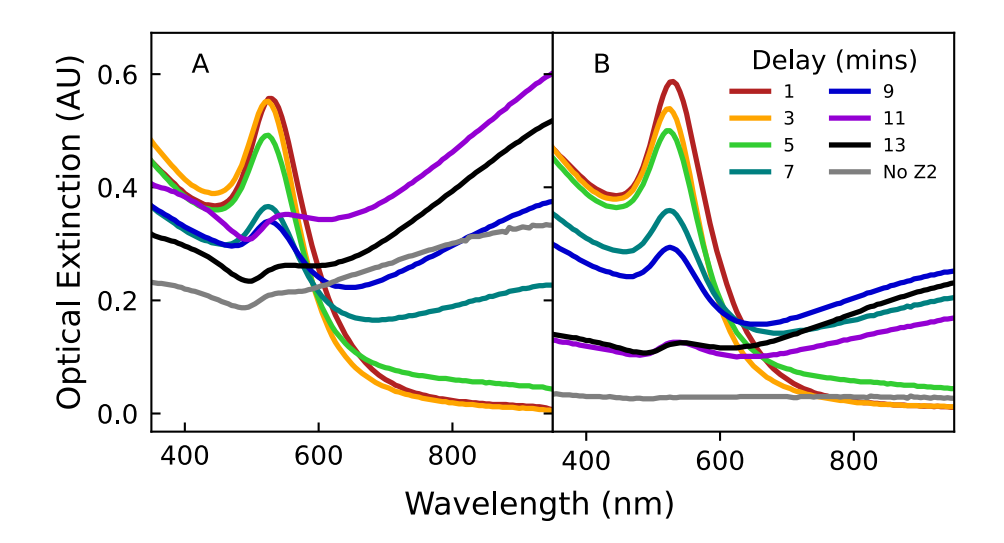


Figure 7: A and B correspond to to spectra taken of samples transferred from the reaction plate immediately after all pipetting commands were finished, and after a delay period of 12-15 hours.

particles were present in addition to spherical particles. However, the broadness of extinction at wavelengths greater than ca. 650 nm, such as when Z2 was added after 7 minutes, suggests that there are multiple in-plane dipolar modes. This can be explained by aggregation, a broad distribution of plate-like particle lateral dimensions, and distinct modes made possible by irregularly shaped particle edges as seen in the work of He and coworkers. We note that the irregular nanoplatelet edges may act as hotspots that enhance their performance in applications such as surface enhanced Raman scattering. Optical extinction in this region of the spectra decreased less significantly than in the control sample, and therefore demonstrates that plate-like particles capped with Z2 are more colloidally stable. Finally, the decrease in optical extinction of the first LSPR peak when Z2 is added after longer delay times indicates that a smaller proportion of spherical particles are formed.

To corroborate these results, a new batch of samples was synthesized and transferred to cuvettes to perform a colloidal stability assay by measuring changes in UV-Vis spectra over the course of 3 days. Changes in absorption at 400 nm and 1000 nm for each sample are shown in Figure 8 A and B to demonstrate changes in overall Au(0) concentration and presence of plate-like particles, respectively. Images of each sample and spectra are included

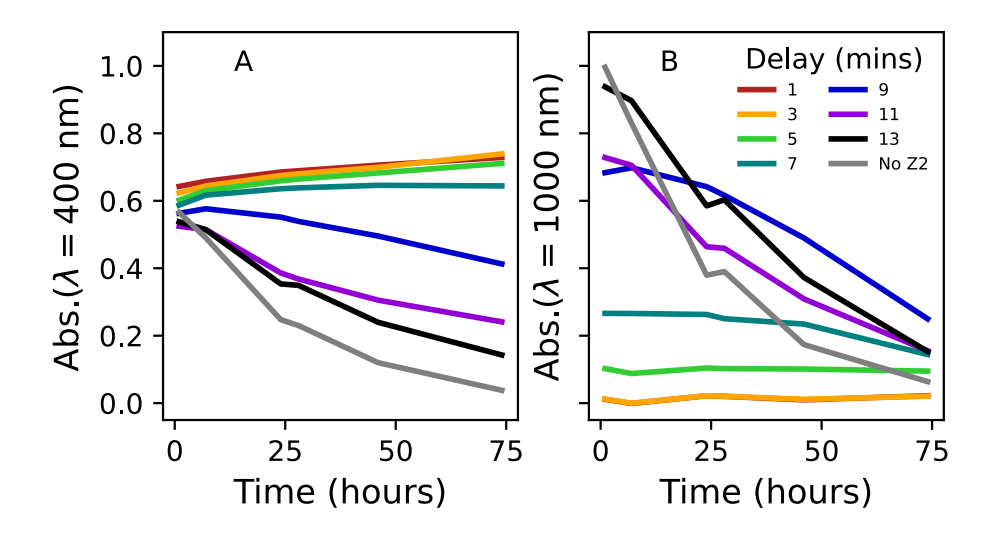


Figure 8: A and B correspond to changes in optical extinction at  $\lambda$ =400 nm and 1000 nm for samples prepared with Z2 being added after different times, or without Z2. Optical extinction at 400 nm is associated with overall Au(0) concentration, <sup>40,47</sup> and optical extinction at 1000 nm is consistent with the presence of plate-like particles. <sup>3,8,42</sup>

in the Supporting Information (Figures S14, S15). Optical extinction at 400 nm increased slightly or remained nearly constant for samples in which Z2 was added after 7 minutes or less. This indicates that the majority of the particles in these conditions remained suspended over the time period of the assay, and are therefore primarily particles small enough for the gravitational force to be negligible relative to random motion. The slight increase over time may be attributed to the slower growth as a result of Au(I)-methionine complexation. The optical extinction at 400 nm decreased most rapidly for the control sample in which no Z2 was added, and is in agreement with the microplate based sedimentation assay. Addition of Z2 after 7 minutes or more produced mixtures of spherical and plate-like particles in which the latter also appeared to sediment. Nevertheless, the optical extinction at 1000 nm shown in Figure 8 B for this set of samples was maintained for a longer time, and was ultimately higher than in the control sample. This shows that the intervention with Z2 was successful at improving the colloidal stability of plate-like particles.

Electron microscopy and AFM were used to directly characterize particle structures formed as a result of intervention. SEM images obtained for samples in which Z2 was

added after 1, 7, 9, and 11 minutes are shown in Figure 9. The addition of Z2 after 1 minute resulted in spherical particles with a diameter of ca. 10 to 30 nm and some nanotriangles. Samples in which Z2 was added at later times feature fewer spherical particles, and more plate-like particles. A more detailed TEM micrograph is also provided in the Supporting Information (Figure S16). The thickness of plate-like particles formed after 7 and 11 minutes was characterized using AFM as shown in the Supporting Information (Figures S3-S7). Several smaller nanoplatelets were identified with a thickness of 10 nm in the former sample, and a larger plate-like structure was found to have a thickness of ca. 12 nm in the latter. These observations confirm that addition of Z2 successfully stabilizes the intermediate plate-like structures from further lateral growth and aggregation.

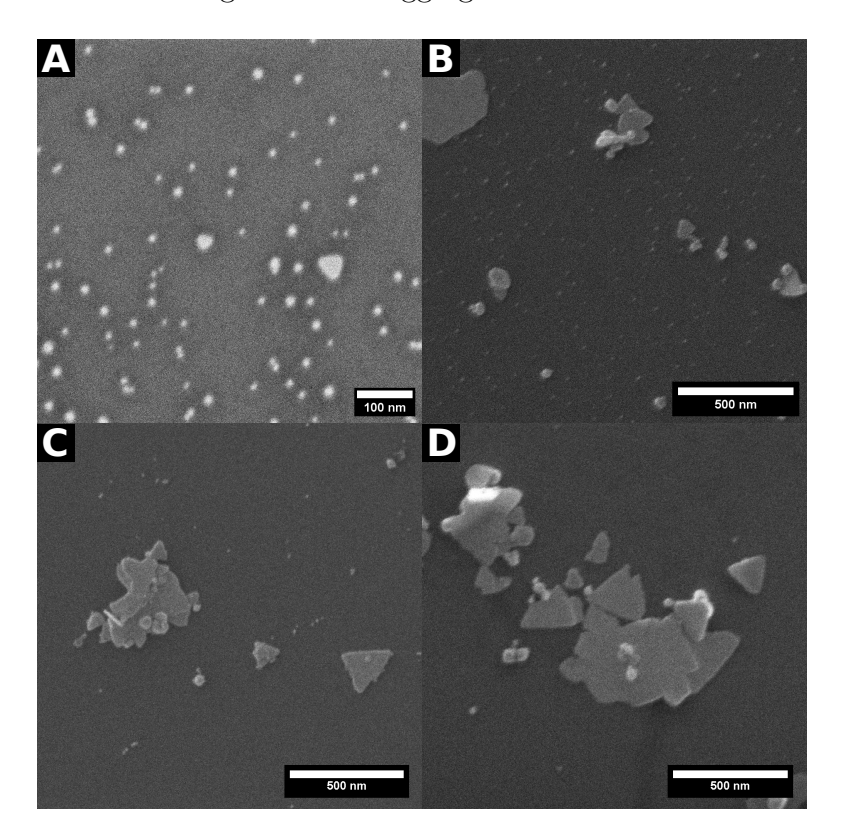


Figure 9: SEM images of Au nanoparticles obtained by mixing in Z2 after different amounts of time. A, B, C, and D correspond to time points of 1, 7, 9, and 11, respectively. The particles in A are primarily spherical particles ranging from ca. 10 to 30 nm in diameter, and some nanotriangles are present. Particles obtained after 7 or 9 minutes also feature some spherical particles, but have a larger proportion of plate-like nanoparticles. Z2 addition after 11 minutes forms primarily plate-like nanoparticles which appear less aggregated than in the control sample with no Z2.

DLS experiments were performed to identify changes in the average size of particles as a result of intervention. The DLS data are presented as an intensity weighted distribution of diffusion coefficients in Figure 10 A. The data is presented in terms of diffusion coefficients, which scale inversely with particle size, because the coexisting spherical and plate-like particle morphologies have different friction coefficients. These data support that a population of more slowly diffusing particles forms when Z2 is added at or after 5 minutes, and that the mean size of this particle population increases when Z2 is added later. The trend in particle size can be estimated as shown in Figure 10 B. The diffusion coefficient of the peak with the largest intensity weighted area for each time of Z2 addition in Figure 10 A is converted to an equivalent diameter depending on the assumed particle morphology. The latter assumption is based on the microscopy results shown in Figure 9 and is described in more detail in the materials and methods section.

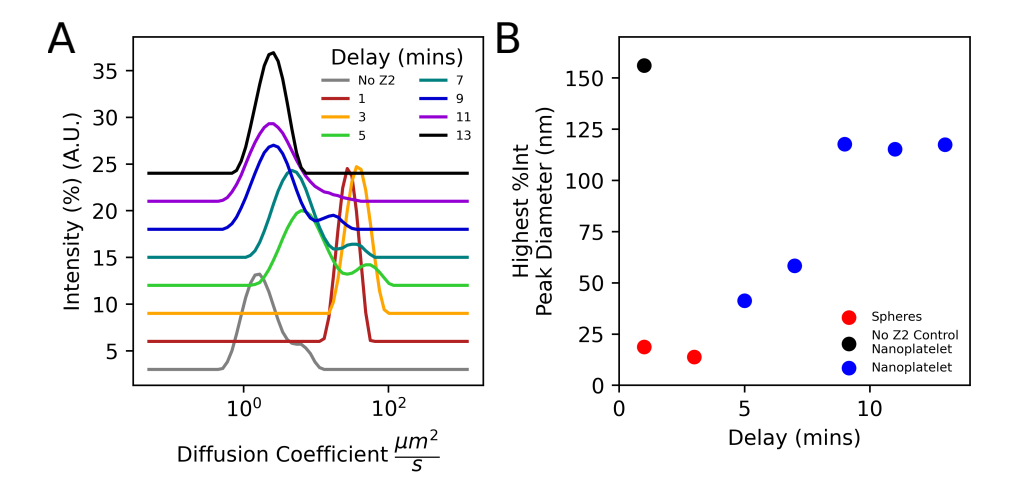


Figure 10: A Intensity weighted distribution of diffusion coefficients for samples in which Z2 was added after a different number of delay times, and for the control sample in which no Z2 is added. B The diffusion coefficients of peaks with the largest intensity weighted area were converted to effective diameters as described in the methods section, and plotted as a function of the delay time.

#### Effect of Z2 Addition on Particle Growth Pathways

In situ UV-Vis measurements were carried out to study the dynamics of particle growth as a result of intervention using Z2. First, the control experiments of particle growth in the presence of just Z2 or Z2M246I are presented in Figure 11. The single LSPR peak and negligible absorption at wavelengths higher than this peak indicate that, in the presence of Z2, dispersed spherical particles were formed without formation of larger clusters, or anisotropic structures. Increased optical absorption at higher wavelengths which then decrease in intensity have been linked to particle clusters and formation of nuclei near the surface of existing particles, i.e. secondary nucleation. <sup>48,49</sup> This shift in optical extinction towards higher wavelengths occurs as a result of plasmonic coupling in metal nanoparticles in close proximity to one another. In the case of the Z2M246I peptide, in the absence of methionine, we observe broad optical absorption and lack of a single LSPR peak. A more defined peak appears after approximately 17 minutes as indicated by the asterisk in Figure 11 B. The initial broad optical extinction is consistent with particles in close proximity, and the later appearance of a distinct peak may be the longitudinal plasmon resonance mode exhibited by nanoplatelets.

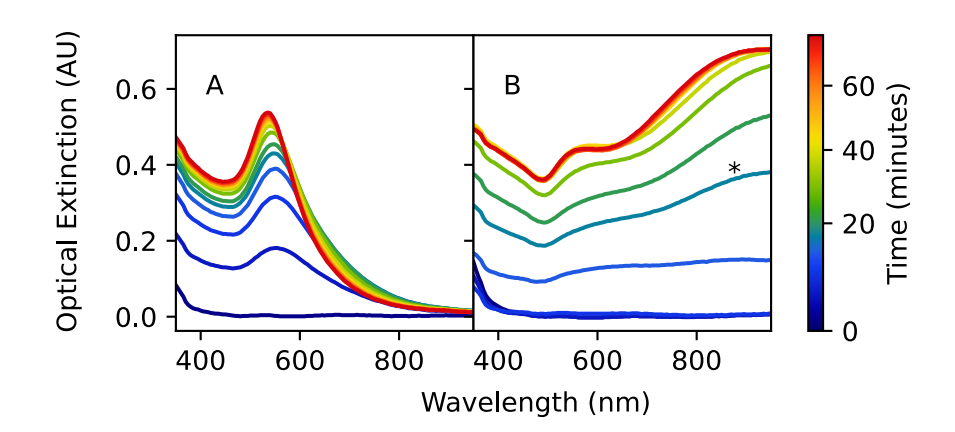


Figure 11: In situ UV-Vis spectra of gold nanoparticle formation over time in the presence of Z2 A, or Z2M246I B. The asterisk in B marks the 17 minute time point at which the prominence of a peak consistent with the longitudinal plasmon resonance mode of plate-like gold particles increases.

Next, we present the *in situ* spectra of Au nanoparticle growth occurring after inter-

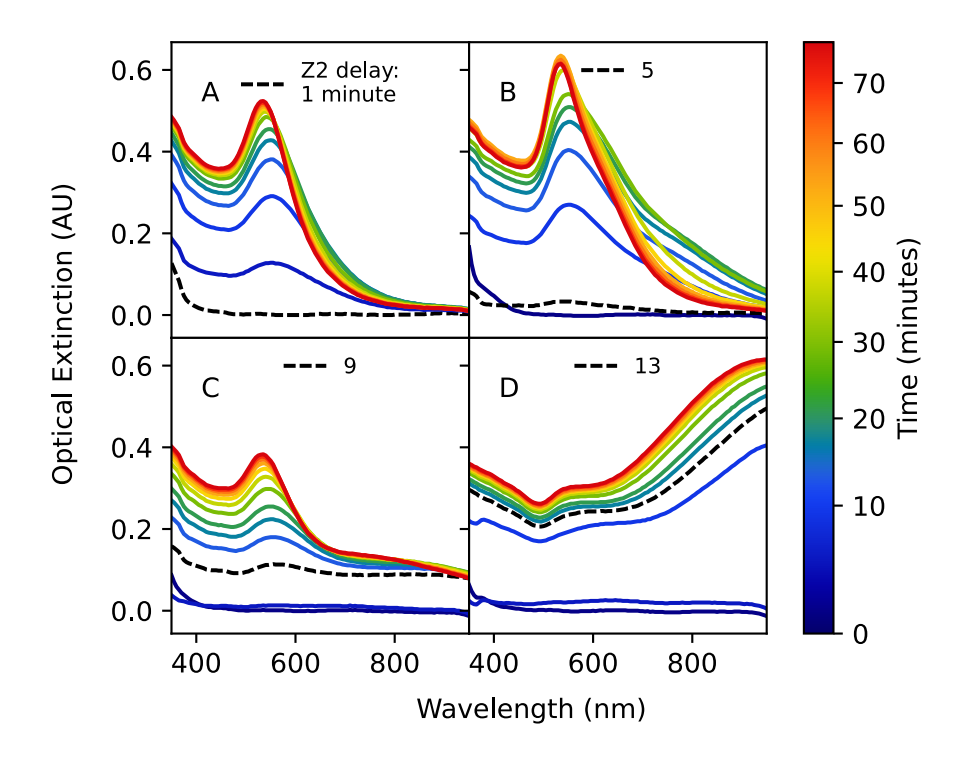


Figure 12: In situ UV-Vis spectra of gold nanoparticle formation over time in which only Z2M246I is present initially, and Z2 is added at different time points: A 1 minute, B 5 minutes, C 9 minutes, D 13 minutes.

vention by addition of Z2 at four different intervals in Figure 12. In the earliest and latest time points, addition of Z2 results in spectra that resemble growth in the presence of Z2 or Z2M246I, respectively. This was expected based on previously discussed imaging and spectroscopy results which showed that the shortest and longest delay times of Z2 addition tended to form structures similar to those found in the presence of either Z2 or Z2M246I on their own. Additionally, we believe that these observations are consistent with Z2 having a higher binding free energy to particle surfaces than Z2M246I. The similarity of the structures formed when Z2 is used on its own to when it is added early on to a synthesis in the presence of Z2M246I resembles the result obtained by Wang et al. <sup>13</sup> The authors demonstrated that replacing a shape-directing molecule with another resulted in unique combinatorial growth pathways only after completing an initial growth stage for a minimum period of time. In our work, growth pathways that were unique from the control experiments featuring either Z2 or Z2M246I were only observed at intermediate time points of Z2 addition. Addition of

Z2 after 5 minutes resulted in spectra consistent with spherical gold nanoparticles, but with additional broad optical extinction at wavelengths greater than the LSPR peak position. The latter broad optical extinction initially increased and then decreased as a function of elapsed time, and suggests that particles were in close proximity to one another at intermediate time points of the reaction and then dispersed. Because HEPES is a weak reducing agent, gold reduction is not yet complete at this time based on the increase in extinction at 400 nm that follows. Therefore, we believe that addition of Z2 at this intermediate time results in complexation of methionine with Au(I), and thereby inhibits secondary nucleation near the surface. <sup>39</sup> Optical extinction at high wavelengths remained relatively constant when Z2 was added 9 minutes after starting the reaction, and the LSPR band from spherical particles continued to grow in intensity. The lack of change in extinction at higher wavelengths suggests that by this point anisotropic particles have already formed, and that there is less Au(I) species for methionine to complex with.

Our experiments demonstrate that dynamic intervention using peptides that have different crystal facet selectivity is a novel method for controlling particle growth. We believe that in addition to differences in facet selectivity between Z2 and Z2M246I, the weak binding free energy that Z2M246I has towards (100) surfaces is a potential reason for formation of highly anisotropic particles. This is suggested by the fact that while Z2 also has a slight preference for (111) facets, spherical particles are primarily formed in the presence of Z2. We anticipate that peptides with a similar ratio of free binding energies to (111) vs. (100) facets, but an overall higher magnitude of binding to (100) facets, would not produce anisotropic materials, with all other factors being equal. Additionally, dynamic intervention together with time-resolved experiments provide unique insights into how nanoplatelets form in the presence of Z2M246I as shown in Figure 13. Exact mechanistic details of particle growth will require additional experimental techniques such as polarized and depolarized DLS, synchrotron quality time-resolved SAXS, and liquid phase TEM. Specifically, it is not clear whether nanoplatelets in the presence of Z2M246I grow laterally via oriented attachment

or fusion along lateral planes, <sup>8,50</sup> or through secondary nucleation due to supersaturation of gold species near the particle surface as discussed by Cheng et al. <sup>49</sup> However, we note that the differences in UV-Vis spectra in Figure 12 with Z2 being added after 5 or 9 minutes are in line with the latter scenario. Substituting methionine for isoleucine resulted in a change in facet selective binding, and allowed for secondary nucleation to take place because Au(I) complexes were not formed with methionine. Facet selective binding of Z2M246I decreases the rate of growth in the [111] direction, <sup>51,52</sup> and secondary nucleation is responsible for lateral growth of existing nanoplatelets. Addition of Z2 at intermediate time points results in equal coverage of nanoplatelet facets, and complexation with Au(I) prevents secondary nucleation near existing nanoplatelets. By removing the bias for growth near existing nanoplatelets, new particles can be formed in the solution and are spherical due to unbiased coverage of facets.

#### Conclusions

This work clarifies the origin of particle anisotropy as a result of methionine substitution in a gold binding peptide, and uses a liquid handling robot to control the dynamics of particle growth through timed intervention. While methionine substitution for isoleucine decreases the overall binding affinity of Z2 variants towards gold surfaces, it also results in appreciable changes in facet selectivity as demonstrated by the results from MD simulations. We note that both an increase in selectivity and an overall decrease in binding energy are responsible for the unique growth pathways observed in the presence of Z2M246I. Based on our in situ SAXS and UV-Vis results we conclude that anisotropic growth likely occurs in clusters where secondary nucleation events extend growth preferentially along the lateral direction of plate-like particles. These secondary nucleation events are suppressed in the presence of methionine, and the presence of facet selective binding peptides changes the rate of growth of different facets. Addition of Z2 at intermediate time points results in pathways in

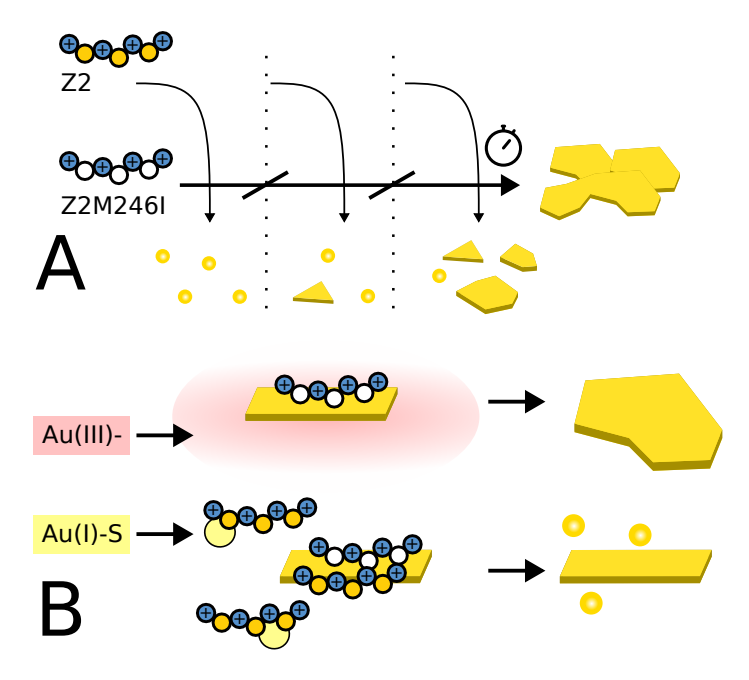


Figure 13: A Timeline of particle growth outcomes when Z2M246I is present from the beginning, and Z2 is added at different times or not added at all. Early addition (e.g. before 3 minutes) leads to spherical particles, intermediate addition times (e.g. more than 3 minutes but less than 11 minutes) lead to a mixture of nanoplatelets with capped growth and spherical particles, and primarily nanoplatelets are obtained in the case of later addition (more than 11 minutes). No intervention with Z2 results in large and aggregated nanoplatelets. B Proposed mechanisms by which Z2 restricts nanoplatelet growth. Enrichment of Au species in the absence of methionine near nanoplatelet surfaces and the preferential adsorption of Z2M246I to (111) facets results in primarily lateral growth of existing nanoplatelets. Addition of Z2 leads to less reactive partially reduced Au(I)-S species formed in complexes with the thioether group of methionines, and thereby limits growth of existing particles via secondary nucleation. Additionally, non-selective adsorption to facets of existing and new particle surfaces biases isotropic growth.

which optical extinction associated with particle aggregation or anisotropy is either reversed, or maintained. The time at which Z2 is introduced controls the proportion of spherical to plate-like nanoparticles, improves the colloidal stability of plate-like particle, and can be used to control the average lateral dimension of plate-like particles. However, identifying exact mechanistic details as a result of dynamic intervention will require in situ characterization such as SAXS or liquid phase TEM combined with a means of mixing reagents at different times, such as with a microfluidic chip. We envision that our experimental automation approach for temporal manipulation of growth pathways can be used by future researchers to achieve control over anisotropic nanoparticle synthesis and other systems.

# Acknowledgement

The presented work was supported by the US Department of Energy (DOE), Office of Science, Office of Basic Energy Sciences (BES), as part of the Energy Frontier Research Centers program: CSSAS - The Center for the Science of Synthesis Across Scales - under award number DE-SC0019288. Part of this work was conducted at the Molecular Analysis Facility, a National Nanotechnology Coordinated Infrastructure (NNCI) site at the University of Washington, which is supported in part by funds from the National Science Foundation (awards NNCI-2025489, NNCI-1542101), the Molecular Engineering & Sciences Institute, and the Clean Energy Institute. Part of this work was conducted with instrumentation provided by the Joint Center for Deployment and Research in Earth Abundant Materials (JCDREAM). This work also benefited from the use of the SasView application, originally developed under NSF award DMR-0520547. SasView also contains code developed with funding from the European Union's Horizon 2020 research and innovation programme under the SINE2020 project, grant agreement No 654000. The authors acknowledge the use of facilities and instrumentation supported by the U.S. National Science Foundation through the Major Research Instrumentation (MRI) program (DMR-2116265) and the UW Molecular Engineering

Materials Center (MEM·C), a Materials Research Science and Engineering Center (DMR-1719797). This work was completed in part through the advanced computational, storage, and networking infrastructure provided by the Hyak supercomputer system and funded by the STF at the University of Washington.

## Supporting Information Available

The following information and results are also available in the online supporting information: additional details about the program used to control the liquid handling robot, a more detailed description of the sample holder used for *in situ* SAXS, additional AFM and TEM results, images and spectra from the cuvette based colloidal stability assay, and additional information about MD simulations. Data and code used to prepare all figures are available on Zenodo (https://doi.org/10.5281/zenodo.8303993)

## References

- Danger, B. R.; Fan, D.; Vivek, J. P.; Burgess, I. J. Electrochemical studies of capping agent adsorption provide insight into the formation of anisotropic gold nanocrystals. ACS Nano 2012, 6, 11018–11026.
- (2) He, Z.; Liu, H.; Tian, Y.; Jiang, Y.; Xu, Y.; Zhan, P.; Wang, M.; Wang, S.; Xia, C.; Gu, C.; Zhao, Z.; Jiang, T.; Zhou, J. Hollow Ag dendritic nanoplates with serrated inner surfaces for sensitive SERS-based detection. *Materials Research Express* 2019, 6.
- (3) O'Brien, M. N.; Jones, M. R.; Kohlstedt, K. L.; Schatz, G. C.; Mirkin, C. A. Uniform circular disks with synthetically tailorable diameters: Two-dimensional nanoparticles for plasmonics. *Nano Letters* **2015**, *15*, 1012–1017.

- (4) He, B.; Wang, Y.; Zhang, M.; Xu, Y.; Zheng, Y.; Liu, X.; Wang, H.; Chen, H. Serrated Au Nanoplates via the Sharpening Etching Mode. *Chemistry of Materials* **2022**, *34*, 8213–8218.
- (5) Gobbo, A.; Marin, R.; Canton, P. Seeded growth of gold nanorods: the effect of sulfur-containing quenching agents. *Journal of Nanoparticle Research* **2018**, *20*, 1–11.
- (6) Zweifel, D. A.; Wei, A. Sulfide-arrested growth of gold nanorods. Chemistry of Materials 2005, 17, 4256–4261.
- (7) Dreaden, E. C.; Alkilany, A. M.; Huang, X.; Murphy, C. J.; El-Sayed, M. A. The golden age: Gold nanoparticles for biomedicine. *Chemical Society Reviews* **2012**, *41*, 2740–2779.
- (8) Ye, S.; Brown, A. P.; Stammers, A. C.; Thomson, N. H.; Wen, J.; Roach, L.; Bushby, R. J.; Coletta, P. L.; Critchley, K.; Connell, S. D.; Markham, A. F.; Brydson, R.; Evans, S. D. Sub-Nanometer Thick Gold Nanosheets as Highly Efficient Catalysts. Advanced Science 2019, 6, 1900911.
- (9) Liu, X.; Wu, D.; Chang, Q.; Zhou, J.; Zhang, Y.; Wang, Z. Grooved nanoplate assembly for rapid detection of surface enhanced Raman scattering. *Nanoscale* **2017**, *9*, 15390–15396.
- (10) Nehra, K.; Pandian, S. K.; Bharati, M. S. S.; Soma, V. R. Enhanced catalytic and SERS performance of shape/size controlled anisotropic gold nanostructures. New Journal of Chemistry 2019, 43, 3835–3847.
- (11) Harutyunyan, H.; Martinson, A. B.; Rosenmann, D.; Khorashad, L. K.; Besteiro, L. V.; Govorov, A. O.; Wiederrecht, G. P. Anomalous ultrafast dynamics of hot plasmonic electrons in nanostructures with hot spots. *Nature Nanotechnology* 2015, 10, 770–774.

- (12) Li, Z.; Zhai, L.; Ge, Y.; Huang, Z.; Shi, Z.; Liu, J.; Zhai, W.; Liang, J.; Zhang, H. Wet-chemical synthesis of two-dimensional metal nanomaterials for electrocatalysis.

  National Science Review 2022, 9, nwab142.
- (13) Wang, Y.; Satyavolu, N. S. R.; Yang, H.; Lu, Y. Kinetic Reconstruction of DNA-Programed Plasmonic Metal Nanostructures with Predictable Shapes and Optical Properties. *Journal of the American Chemical Society* **2022**, *144*, 4410–4421.
- (14) Lachowski, K. J.; Vaddi, K.; Naser, N. Y.; Baneyx, F.; Pozzo, L. D. Multivariate analysis of peptide-driven nucleation and growth of Au nanoparticles. *Digital Discovery* 2022, 1, 427–439.
- (15) Abarca, C.; Ali, M. M.; Yang, S.; Dong, X.; Pelton, R. H. A Colloidal Stability Assay Suitable for High-Throughput Screening. *Analytical Chemistry* **2016**, *88*, 2929–2936.
- (16) Peelle, B. R.; Krauland, E. M.; Wittrup, K. D.; Belcher, A. M. Design Criteria for Engineering Inorganic Material- Specific Peptides. *Langmuir* **2005**, *21*, 6929–6933.
- (17) Hammouda, B. A new Guinier-Porod model. *Journal of Applied Crystallography* **2010**, 43, 716–719.
- (18) Doucet, M. et al. SasView version 5.0.4. Accessed 2022-05-01.
- (19) Nečas, D.; Klapetek, P. Gwyddion: an open-source software for SPM data analysis. Central European Journal of Physics 2012, 10, 181–188.
- (20) Hernández-Cifre, J. G.; Rodríguez-Schmidt, R.; Almagro-Gómez, C. M.; García de la Torre, J. Calculation of the friction, diffusion and sedimentation coefficients of nanoplatelets of arbitrary shape. *Polymer* 2022, 262, 125467.
- (21) Dennington, R.; Keith, T. A.; Millam, J. M. GaussView Version 6. 2019; Semichem Inc. Shawnee Mission KS.

- (22) Qi, X.; Jin, B.; Cai, B.; Yan, F.; De Yoreo, J.; Chen, C.-L.; Pfaendtner, J. Molecular Driving Force for Facet Selectivity of Sequence-Defined Amphiphilic Peptoids at Au-Water Interfaces. *The Journal of Physical Chemistry B* **2022**, *126*, 5117–5126.
- (23) Huang, J.; MacKerell, A. D. CHARMM36 all-atom additive protein force field: Validation based on comparison to NMR data. *Journal of Computational Chemistry* **2013**, 34, 2135–2145.
- (24) Vanommeslaeghe, K.; Hatcher, E.; Acharya, C.; Kundu, S.; Zhong, S.; Shim, J.; Darian, E.; Guvench, O.; Lopes, P.; Vorobyov, I.; Mackerell, A. D. CHARMM general force field: A force field for drug-like molecules compatible with the CHARMM all-atom additive biological force fields. *Journal of Computational Chemistry* **2009**, NA–NA.
- (25) Wright, L. B.; Rodger, P. M.; Corni, S.; Walsh, T. R. GolP-CHARMM: First-Principles Based Force Fields for the Interaction of Proteins with Au(111) and Au(100). *Journal of Chemical Theory and Computation* **2013**, *9*, 1616–1630.
- (26) Jorgensen, W. L.; Chandrasekhar, J.; Madura, J. D.; Impey, R. W.; Klein, M. L. Comparison of simple potential functions for simulating liquid water. The Journal of Chemical Physics 1983, 79, 926–935.
- (27) Martínez, L.; Andrade, R.; Birgin, E. G.; Martínez, J. M. PACKMOL: A package for building initial configurations for molecular dynamics simulations. *Journal of Computational Chemistry* **2009**, *30*, 2157–2164.
- (28) Abraham, M. J.; Murtola, T.; Schulz, R.; Páll, S.; Smith, J. C.; Hess, B.; Lindahl, E. GROMACS: High performance molecular simulations through multi-level parallelism from laptops to supercomputers. *SoftwareX* **2015**, *1-2*, 19–25.
- (29) Tribello, G. A.; Bonomi, M.; Branduardi, D.; Camilloni, C.; Bussi, G. PLUMED 2: New feathers for an old bird. *Computer Physics Communications* **2014**, *185*, 604–613.

- (30) Bussi, G.; Donadio, D.; Parrinello, M. Canonical sampling through velocity rescaling.

  The Journal of Chemical Physics 2007, 126, 014101.
- (31) Berendsen, H. J. C.; Postma, J. P. M.; van Gunsteren, W. F.; DiNola, A.; Haak, J. R. Molecular dynamics with coupling to an external bath. The Journal of Chemical Physics 1984, 81, 3684–3690.
- (32) Pfaendtner, J.; Bonomi, M. Efficient Sampling of High-Dimensional Free-Energy Landscapes with Parallel Bias Metadynamics. *Journal of Chemical Theory and Computation* **2015**, *11*, 5062–5067.
- (33) Raiteri, P.; Laio, A.; Gervasio, F. L.; Micheletti, C.; Parrinello, M. Efficient Reconstruction of Complex Free Energy Landscapes by Multiple Walkers Metadynamics.

  The Journal of Physical Chemistry B 2006, 110, 3533–3539.
- (34) Branduardi, D.; Bussi, G.; Parrinello, M. Metadynamics with Adaptive Gaussians.

  Journal of Chemical Theory and Computation 2012, 8, 2247–2254.
- (35) The PLUMED consortium, Promoting transparency and reproducibility in enhanced molecular simulations. *Nature Methods* **2019**, *16*, 670–673.
- (36) Tang, Z.; Palafox-Hernandez, J. P.; Law, W.-C.; Hughes, Z. E.; Swihart, M. T.; Prasad, P. N.; Knecht, M. R.; Walsh, T. R. Biomolecular Recognition Principles for Bionanocombinatorics: An Integrated Approach To Elucidate Enthalpic and Entropic Factors. ACS Nano 2013, 7, 9632–9646.
- (37) Tan, Y. N.; Lee, J. Y.; Wang, D. I. Uncovering the design rules for peptide synthesis of metal nanoparticles. *Journal of the American Chemical Society* **2010**, *132*, 5677–5686.
- (38) Isab, A. A.; Sadler, P. J. Reactions of gold(III) ions with ribonuclease A and methionine derivatives in aqueous solution. *BBA Protein Structure* **1977**, *492*, 322–330.

- (39) Sahu, J. K.; Lone, S. A.; Sadhu, K. K. Methionine-Controlled Impediment of Secondary Nucleation Leading to Nonclassical Growth within Self-Assembled De Novo Gold Nanoparticles. *Langmuir* **2022**, *38*, 5865–5873.
- (40) Hendel, T.; Wuithschick, M.; Kettemann, F.; Birnbaum, A.; Rademann, K.; Polte, J. In Situ Determination of Colloidal Gold Concentrations with UV-Vis Spectroscopy: Limitations and Perspectives. Analytical Chemistry 2014, 86, 11115–11124.
- (41) Germain, V.; Li, J.; Ingert, D.; Wang, Z. L.; Pileni, M. P. Stacking faults in formation of silver nanodisks. *Journal of Physical Chemistry B* **2003**, *107*, 8717–8720.
- (42) Tan, T.; Zhang, S.; Wang, J.; Zheng, Y.; Lai, H.; Liu, J.; Qin, F.; Wang, C. Resolving the stacking fault structure of silver nanoplates. *Nanoscale* **2021**, *13*, 195–205.
- (43) Heinz, H.; Farmer, B. L.; Pandey, R. B.; Slocik, J. M.; Patnaik, S. S.; Pachter, R.; Naik, R. R. Nature of molecular interactions of peptides with gold, palladium, and Pd-Au bimetal surfaces in aqueous solution. *Journal of the American Chemical Society* 2009, 131, 9704–9714.
- (44) Prasad, J.; Viollet, S.; Gurunatha, K. L.; Urvoas, A.; Fournier, A. C.; Valerio-Lepiniec, M.; Marcelot, C.; Baris, B.; Minard, P.; Dujardin, E. Directed evolution of artificial repeat proteins as habit modifiers for the morphosynthesis of (111)-terminated gold nanocrystals. *Nanoscale* 2019, 11, 17485–17497.
- (45) Mao, C. M.; Sampath, J.; Sprenger, K. G.; Drobny, G.; Pfaendtner, J. Molecular Driving Forces in Peptide Adsorption to Metal Oxide Surfaces. *Langmuir* 2019, 35, 5911–5920.
- (46) Hughes, Z. E.; Kochandra, R.; Walsh, T. R. Facet-Specific Adsorption of Tripeptides at Aqueous Au Interfaces: Open Questions in Reconciling Experiment and Simulation. Langmuir 2017, 33, 3742–3754.

- (47) Khlebtsov, N. G.; Khlebtsov, B. N.; Kryuchkova, E. V.; Zarkov, S. V.; Burov, A. M. Universal Determination of Gold Concentration in Colloids with UV-vis Spectroscopy. The Journal of Physical Chemistry C 2022, 126, 19268–19276.
- (48) Andalibi, M. R.; Wokaun, A.; Bowen, P.; Testino, A. Kinetics and Mechanism of Metal Nanoparticle Growth via Optical Extinction Spectroscopy and Computational Modeling: The Curious Case of Colloidal Gold. *ACS Nano* **2019**, *13*, 11510–11521.
- (49) Cheng, Y.; Tao, J.; Zhu, G.; Soltis, J. A.; Legg, B. A.; Nakouzi, E.; De Yoreo, J. J.; Sushko, M. L.; Liu, J. Near surface nucleation and particle mediated growth of colloidal Au nanocrystals. *Nanoscale* 2018, 10, 11907–11912.
- (50) Kim, M. H.; Yoon, D. K.; Im, S. H. Growth pathways of silver nanoplates in kinetically controlled synthesis: bimodal versus unimodal growth. *RSC Advances* **2015**, *5*, 14266–14272.
- (51) Li, Y.; Lin, H.; Zhou, W.; Sun, L.; Samanta, D.; Mirkin, C. A. Corner-, edge-, and facet-controlled growth of nanocrystals. *Science Advances* **2021**, *7*, 1–7.
- (52) Xia, Y.; Xia, X.; Peng, H. C. Shape-Controlled Synthesis of Colloidal Metal Nanocrystals: Thermodynamic versus Kinetic Products. *Journal of the American Chemical Society* 2015, 137, 7947–7966.